Hydration kinetics and products of MgO-activated blast furnace slag

Solmoi Park [a,b], Hyeong Min Park [c,d], H.N. Yoon [b], Joonho Seo [b], Cheol-Min Yang [d], John L. Provis [e], Beomjoo Yang [c,*]

[a] Department of Civil Engineering, Pukyong National University, 45 Yongso-ro, Nam-gu, Busan 48513, Republic of Korea
[b] Department of Civil and Environmental Engineering, Korea Advanced Institute of Science and Technology, 291 Daehak-ro, Yuseong-gu, Daejeon 34141, Republic of Korea
[c] School of Civil Engineering, Chungbuk National University, Chungdae-ro 1, Seowon-gu, Cheongju, Chungbuk 28644, Republic of Korea
[d] Institute of Advanced Composite Materials, Korea Institute of Science and Technology (KIST), 92 Chudong-ro, Bongdong-eup, Wanju-gun Jeonbuk 55324, Republic of Korea
[e] Department of Materials Science & Engineering, The University of Sheffield, Sheffield S1 3JD, United Kingdom

HIGHLIGHTS

- The hydration kinetics of MgO-activated blast furnace slag is studied.
- The main hydration products include a C-A-S-H type gel, ettringite, monosulfate, hydrotalcite, and TAH.
- Higher MgO increases the degree of reaction of slag.
- Higher MgO increases the solid binder volume, and the strength of the samples.

ARTICLE INFO

ABSTRACT

Hydration kinetics and products of MgO-activated slag are investigated by employing multiple analytical characterization techniques and thermodynamic modelling. The main hydration products of this cement are a calcium-aluminosilicate hydrate type gel, ettringite, monosulfate, hydrotalcite, brucite, and a third aluminate hydrate, while the extent of reaction and formation of reaction products significantly varied by MgO dosages. Higher dosage of MgO increased the degree of reaction of slag, and led to a higher population of Al in the octahedral region, which can be attributed to greater competition for Al required for the formation of hydrotalcite. The experimental and simulated volume of the solid binder increased as the MgO dosage increased, showing a good correlation with the strength increase of the samples with higher MgO dosage.

1. Introduction

Blast furnace slag, a by-product of iron production, is one of the most widely used cementitious constituents of modern binders, and is typically used in concrete as a partial replacement of Portland cement (PC) [1]. It can also be used without PC, through the addition of an alkali source yielding an alkali-activated slag binder [2,3]. Slag-derived binders, activated using PC or other sources of activators, play an important role in the construction industry, not solely because of their improved durability performance [4–6], but also due to their reduced attributed environmental footprint compared to PC.

The chemistry of slag-derived binders is strongly influenced by the selection of the activator [7–9]. The main reaction product of

slag-blended PC is a C-A-S-H gel, while the formation of secondary phases depends on the slag:PC ratio; increasing the slag content in slag-PC blends leads to a decrease in portlandite and ettringite content, and an increase in hydrotalcite [10,11]. Alkali-containing C-A-S-H (often represented as C-(N-)A-S-H using Na as the archetypal alkali metal) is the main reaction product in alkali-activated slag binders [12]. Similarly, the main reaction product of slag activated with near-neutral salts [13] or alkali-earth metal oxides [14,15] is a C-A-S-H type gel, while the secondary phases formed in the binder are dependent on the anions provided by the activator, i.e., Na_2SO_4-activated slag shows notable quantities of ettringite [16,17], and calcium carbonates and gaylussite are formed at early age in the system activated with Na_2CO_3 [18].

The microstructural features and durability performance of slag binders are strongly associated with the binding phases present [19]. This means that the MgO supplied by the slag plays an important role in determining the characteristics of slag-derived binders,

because its presence within slag glass can enhance the reaction kinetics of the slag [20,21], and arguably more importantly, because it leads to the formation of Mg-Al layered double hydroxides as secondary phases, and these factors to a significant extent govern the durability performance of concretes produced from these binders [22,23]. In particular, alkali-activated slags with higher amounts of MgO supplied by the precursor, or with certain dosages of externally added MgO, have shown improved resistance to carbonation [24,25] and to chloride ingress [26,27]. For this reason, work has been conducted where MgO is used as an activator (or part of a multi-constituent activator) for blast furnace slag [28–31]. Binders derived from slag activated by MgO are reported to exhibit mechanical properties that meet the requirements for use as construction materials, and consist of C-A-S-H as a primary reaction product in addition to a hydrotalcite-like phase [28–30]. However, the detailed chemistry and quantitative structural information of this type of binder are yet to be fully revealed.

This study presents a detailed investigation of the hydration kinetics and products of MgO-activated slag. Blast furnace slag with a very low content of MgO (~3%) was obtained to explore its hydration behavior with the addition of supplemental MgO in the form of the activator; it is expected that there will be differences in material performance and hydration pathways in this system where the MgO is supplied as a rapidly-reacting activator separately from the slag glass, compared to the more usual case where MgO is released along with other binder constituents as the slag dissolves into the alkaline environment of the activating solution.

2. Experimental procedure

2.1. Materials and sample preparation

The chemical composition of the blast furnace slag used in this study as obtained by the X-ray fluorescence analysis is shown in Table 1. The Rietveld refinement-based quantitative analysis of the X-ray diffraction (XRD) pattern of the slag revealed that it consists of 0.5% portlandite, 0.5% lime, 1.2% calcite, 2.1% anhydrite and 95.7% amorphous phase. MgO (light-burned, 96% purity, and reactivity of 29.3 s in accordance with the acetic acid test [32]) was added at dosages of 0, 5%, 10%, and 20% by mass of the binder materials (slag + MgO). The particle size distributions of the raw materials are shown in Fig. 1. The BET surface area of the slag and MgO was 0.896 and 37.3 m^2/g. The water-to-binder ratio was kept constant at 0.40 for all mixtures. The samples were prepared by dry-mixing the binder materials, and then adding deionized water. The mixtures were mechanically stirred for five minutes to ensure homogeneity. The fresh paste was poured into a mold, which was then sealed with a plastic bag. The samples were cured at 20 °C and 60% relative humidity until the designated test day.

2.2. Test methods

MgO-activated slag specimens were characterized by compressive strength testing, and then sample fragments retrieved after compressive strength tests were immersed in isopropanol and des-
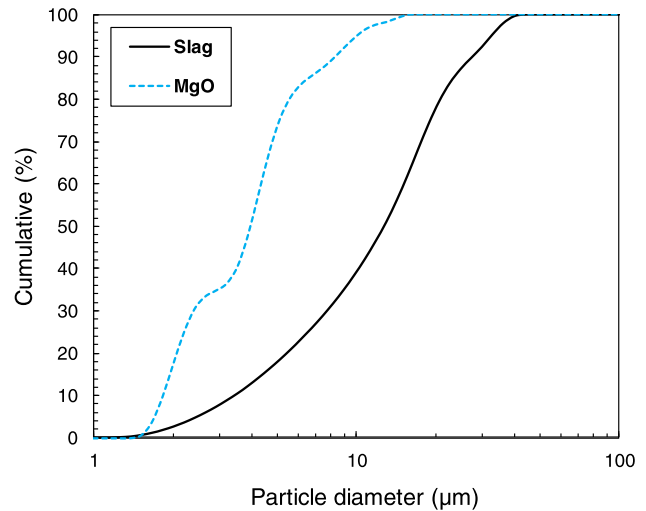

Fig. 1. Particle size distribution of raw materials used in this study. The dv(50) of the slag and MgO was 14.0 and 4.3 μm, respectively.

iccated under vacuum to arrest hydration after 28 days of curing. The samples were ground to pass a 64 μm sieve where samples needed to be powdered. The characterization tools applied were mercury intrusion porosimetry (MIP), XRD, thermogravimetry (TG), and solid-state magic angle-spinning nuclear magnetic resonance (MAS NMR) spectroscopy. The following conditions were employed for the analyses:

- XRD: using a Rigaku SmartLab (Rigaku Corp.) instrument by employing CuKα radiation at 45 kV and 200 mA, a step size of 0.02, and a counting time of 1 s per step.
- TG: on a TA Instrument Q600 device (PH 407), employing a heating rate of 10 °C/min between 40 and 1000 °C in an N$_2$ environment.
- Solid-state ^{29}Si MAS NMR spectroscopy: using an Avance III HD Instrument (9.4 T, Bruker, Germany). A transmitter frequency of 79.51 MHz, pulse length of 30° (2.2 μs), spinning rate of 6 kHz, and relaxation delay of 22 s, a 5 mm HX-CPMAS probe and 5 mm zirconia rotor were used for acquisition of ^{29}Si MAS NMR spectra. A transmitter frequency of 156.32 MHz, pulse length of 30° (1.8 μs), spinning rate of 22 kHz, and relaxation delay of 2 s, a 2.5 mm HX-CPMAS probe and 2.5 mm low Al zirconia rotor were used for acquisition of ^{27}Al MAS NMR spectra. The chemical shifts were referenced to TMS at 0 ppm and aqueous AlCl$_3$ at 0 ppm, respectively.
- MIP: using an Autopore VI 9500 (Micromeritics Instrument Corp.) by applying a pressure range of 0.2–413.7 MPa (30–60,000 psia) during the intrusion and extrusion of mercury.
- Compressive strength tests: using an Instron 5985 instrument (INSTRON) by employing a loading rate of 0.2 mm/s on three 25 mm cubic paste samples.

The phase assemblage of MgO-activated slag was modelled using the Gibbs energy minimization software GEM-Selektor v.3.5 (http://gems.web.psi.ch/) [33–35], coupled with the

Table 1
Chemical composition of slag used in this study. All elements are represented in oxide form regardless of their oxidation state in the original slag.

(wt%)	CaO	SiO$_2$	Al$_2$O$_3$	MgO	Na$_2$O	K$_2$O	SO$_3$	Fe$_2$O$_3$	TiO$_2$	Mn$_2$O$_3$	SrO	LOI*
Slag	44.8	33.5	13.7	2.9	0.2	0.5	1.7	0.5	0.5	0.2	0.1	1.4

* Loss on ignition, determined in accordance with ASTM C114.

Cemdata18 database [36]. The modelling was commenced using 100 g of binder materials in which the MgO activator, and the CaO, SiO_2, Al_2O_3, and MgO contained in the slag, were assumed to be reactive components [7,12]. The total amount of the mineralogical phases identified by the quantitative XRD analysis of raw slag (lime, portlandite, anhydrite, calcite) were added to the system regardless of the reaction degree of the slag. The amount of SO_3 obtained by the XRF analysis was assumed to originate from the presence of anhydrite only. The residual amount of MgO as quantified by the quantitative XRD analysis was subtracted from the amount of MgO being introduced to the modelled system. The activity coefficients of aqueous phases were calculated using the extended Debye-Hückel equation [37], assuming a KOH-dominated background electrolyte.

3. Results

3.1. XRD

The XRD patterns of the MgO-activated slag are shown in Fig. 2. The XRD pattern of the raw slag showed peaks corresponding to the presence of calcite ($CaCO_3$, PDF# 5–586), anhydrite ($CaSO_4$, PDF# 37–1496), lime (CaO, PDF# 43–1001), and portlandite (Ca$(OH)_2$, PDF# 4–733). The anhydrite appears to have been interground with the slag according to industrial practice in some parts of the world, and the portlandite is likely to have arisen from atmospheric hydration of the free lime present.

The presence of C-S-H type gels in all activated samples is noted by weak Bragg reflections due to structural similarities with tobermorite ($Ca_5(Si_6O_{16})(OH)_2$, PDF# 01–089-6458), and these gels are expected to have some degree of Al substitution in the Si sites [38], although this cannot be unequivocally determined from the XRD data presented here. Calcite persists in the activated samples, and ettringite ($Ca_6Al_2(SO_4)_3(OH)_{12}\cdot26(H_2O)$, PDF# 41–1451) is observed in all samples, while the peaks related to AFm phases such as monosulfate ($Ca_4Al_2(OH)_{12}(S_{0.5}O_2(OH_2)_6)$, PDF# 01–083-1289) are identifiable in all samples with up to 10% MgO, and hemicarbonate ($Ca_4Al_2O_7(CO_2)_{0.5}\cdot14H_2O$, PDF# 41–0221) is also present in the 0% MgO sample.

On the other hand, the samples with higher dosages of MgO showed peaks due to brucite ($Mg(OH)_2$, PDF# 7–239), and the evolution of a layered double hydroxide (LDH) phase that shares structural similarities with hydrotalcite ($Mg_6Al_2CO_3(OH)_{16}\cdot4H_2O$, PDF# 00–022-0700). As depicted in Fig. 2 (c) the LDH phases in the low-MgO samples are AFm-structured monosulfate and hemicarbonate, while the LDH phases in the high-MgO samples are in the hydrotalcite group. Meanwhile, the Rietveld refinement-based quantitative XRD analysis of the samples with MgO showed that 18%, 16% and 13% of the MgO was not hydrated in the 5%, 10% and 20% MgO samples, showing that a minor quantity of MgO remained in the binder matrix.

The formation of ettringite appears to be unaffected by the incorporation of MgO, since all samples showed peaks of similar magnitude that are assigned to ettringite. It is important to note that ettringite formation in slag-based binders is greatly dependent on the chemistry of the slag; ettringite is absent from alkali-activated slag incorporating MgO [30] or MgO-activated slag [31] when the slag used does not contain a noticeable amount of sulfate. In contrast, ettringite is identified as the main hydration product in commercial slags that contain calcium sulfate or gypsum and are hydrated without the aid of chemical activators [39], and is also predicted in thermodynamic simulations of phase assemblages resulting from alkali-activation across quite a wide range of slag compositions [12]. It is interesting that the role of Mg in alkali-activated slags has been identified to include a signif-
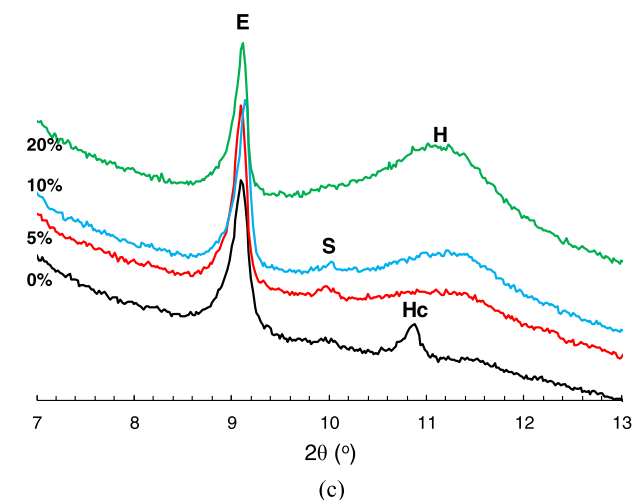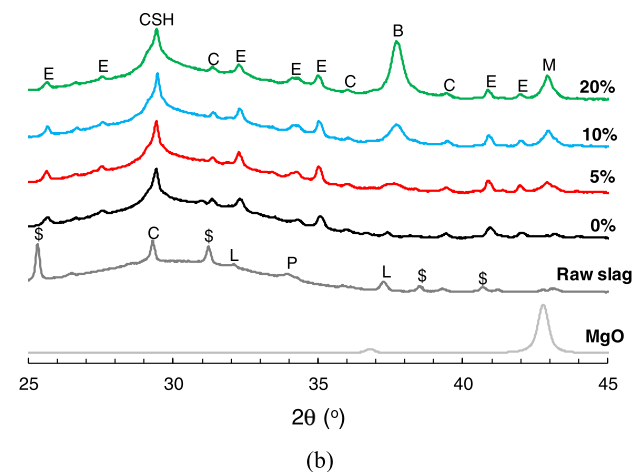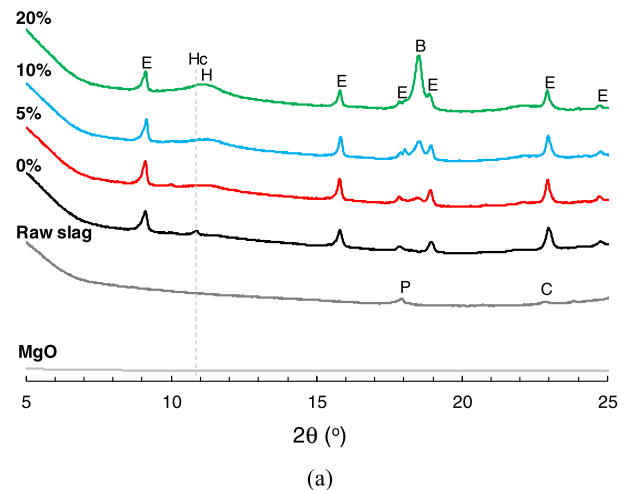

Fig. 2. XRD patterns of MgO-activated slag at (a) 5-25° 2θ, (b) 25-45° 2θ, and (c) 7-13° 2θ where peaks due to Al-bearing phases are particularly identifiable. The annotations indicate: M- MgO, P- portlandite, $- anhydrite, L- lime, C- calcite, B-brucite, CSH- C-S-H type gel, E- ettringite, H- hydrotalcite, Hc- hemicarbonate, and S- monosulfate.

icant degree of control over the availability of Al for incorporation into C-S-H type gels and other phases, but its addition here does not appear to reduce Al availability to a degree that influences ettringite formation.

3.2. TG/DTG

The TG and the derivative TG (DTG) curves of the MgO-activated slag are shown in Fig. 3. All samples showed DTG peaks at 90 °C due to the evaporation of physically absorbed water from C-S-H type gels [40], and at 680 °C due to decarbonation of calcite [41,42]. The samples with MgO showed increasing intensity of the DTG peak at 60 °C and of the shoulder at 100–200 °C as MgO was added. These peaks are attributed to the removal of absorbed and interlayer water, respectively, from LDH phases [43]. It can be inferred that the formation of hydration products in these samples, namely C-A-S-H, AFt and AFm phases, was enhanced by increased dosage of MgO.

These samples also showed a peak from 260 to 450 °C, centered at 360–400 °C, which shifted toward higher temperatures as the MgO dosage increased. Considering that dehydroxylation of hydrotalcite and brucite occur at 310 °C [43] and 400 °C [44], respectively, the decomposition processes of these two phases can be reflected by the DTG peak at this position, and indicates that the increased MgO dosage in the samples led to more hydrotalcite and brucite being formed in the samples.
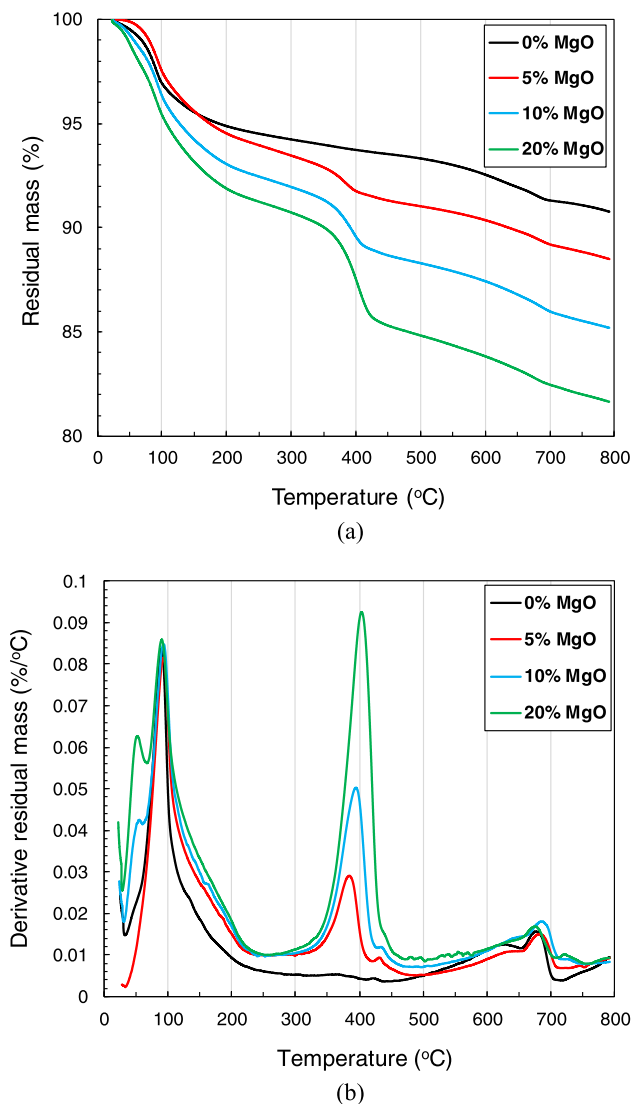
3.3. Solid-state ^{27}Al MAS NMR spectroscopy

The ^{27}Al MAS NMR spectra of the MgO-activated slag are shown in Fig. 4. The melilite-like glassy network of slag is often characterized by a broad resonance centered at 65 ppm due to the presence of tetrahedral Al sites [45]. New resonances with varying intensity depending on the samples are observed at 52 to 80 ppm and −10 to 15 ppm in the spectra of the 0, 5, 10 and 20% MgO samples, due to the presence of tetrahedral Al in C-S-H type gels (C-A-S-H) [47–49] and octahedral sites in AFt/AFm and hydrotalcite-group phases [39,50,62], respectively.

The intensity of the resonance due to the tetrahedral sites was significantly reduced by higher MgO dosage, indicating a potential decrease in the Al in unreacted slag as the activation increased the extent of reaction, and in C-A-S-H as there was greater competition for Al due to the formation of the hydrotalcite-like LDH. Correspondingly, an increase in intensity was observed in the octahedral region, and the increase in the resonance at 9–10 ppm due to the presence of hydrotalcite-type LDH structures (which also overlaps with an AFm contribution) was particularly notable. While this observation is in agreement with the XRD pattern showing increased peak intensity of hydrotalcite upon increased MgO dosage in the samples, the intensity of the resonance assigned to ettringite at 13 ppm [50] was relatively lower as the intensity of hydrotalcite and the MgO dosage in the samples increased. Hence, the ^{27}Al MAS NMR spectra of the MgO samples provided more detailed information regarding the local Al environment in addition to what was obtained from the XRD analysis. The spectra of the MgO samples also showed resonance at 6–7 ppm which is closely associated with the presence of third aluminate hydrate [45].

3.4. Solid-state ^{29}Si MAS NMR spectroscopy

The ^{29}Si MAS NMR spectra of the MgO-activated slag are shown in Fig. 5, and the deconvolution results of the spectra are summarized in Table 2. The deconvolution was performed using the
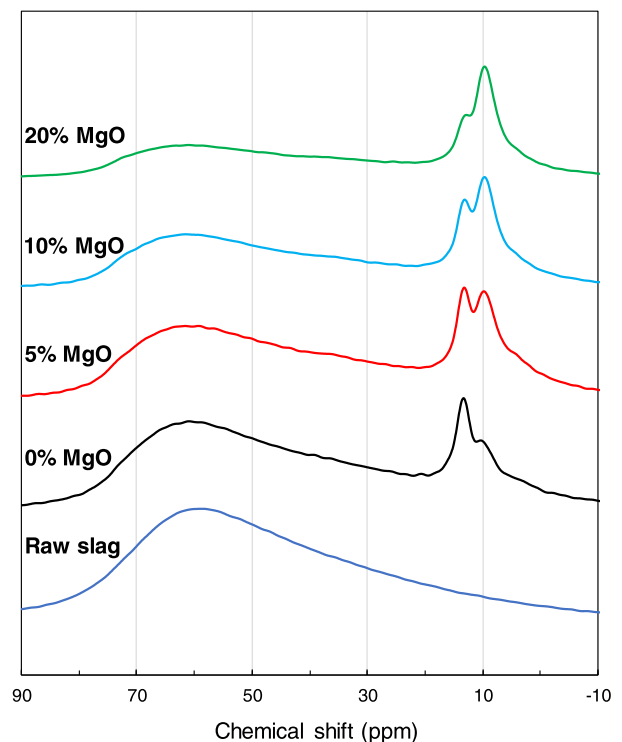

Fig. 3. (a) TG and (b) DTG curves of MgO-activated slag.

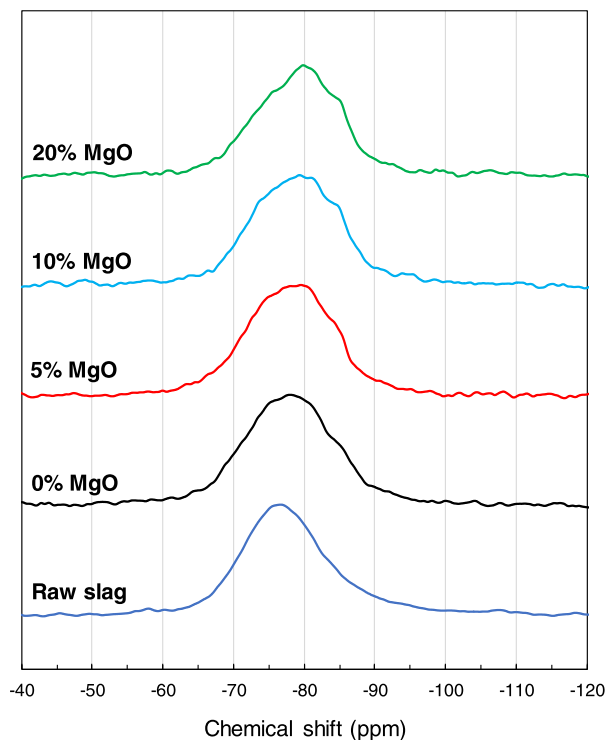**Fig. 4.** ^{27}Al MAS NMR spectra of MgO-activated slag.

Fig. 5. ^{29}Si MAS NMR spectra of MgO-activated slag samples.

OriginPro 9 software by introducing component peaks at site locations identified in previous studies [46,51–54,63,64], with the width of each peak (FWHH) constrained to be no more than 5 ppm. The resonance of the raw slag was simulated using the Gaussian LorenCross function, and it was able to be well described by a single peak of this shape, while the Si sites in C-A-S-H were modelled using Gaussian functions.

The relative areas of the unreacted slag contributions to the spectra of the samples with 0% and 5% MgO after 28 days of hydration were 85% and 86%, showing the unactivated slag and that at this low MgO dose have similar reactivity. For the other samples with higher MgO dosages, there was a clear increase in the reaction degree. This is in fair agreement with the ^{27}Al MAS NMR spectra which showed a reduction in the intensity of the resonance assigned to the unreacted slag upon the addition of MgO. Although the reaction degree of slag in alkali-activated binders varies greatly depending on the precursor and activator chemistry and the slag fineness, it has been reported as 76% [45], 52–55% [54], and 32–38% [55] at a similar sample age as in this study (28 days) when estimated using NMR and scanning electron microscopy-based image analysis techniques. The reaction degrees of the 10% and 20% MgO samples (38% and 42%, respectively) at 28 days were similar to the samples activated with a near-neutral salt activator (sodium carbonate), which was 36–59% [20] at a similar sample age.
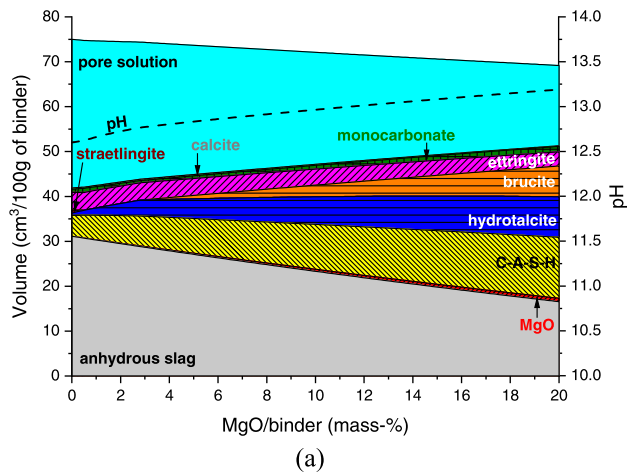
The spectra of 10% and 20% MgO samples showed non-zero resonance contributions from Q^2, Q^3(1Al) and Q^4(nAl) sites, while those of the other samples approached zero in the chemical shift range corresponding to these sites. This implies that the bridging sites in C-A-S-H chains of the 0% and 5% MgO samples are occupied by Al (as all of the mid-chain sites identified were in Q^2(1Al) coordination).
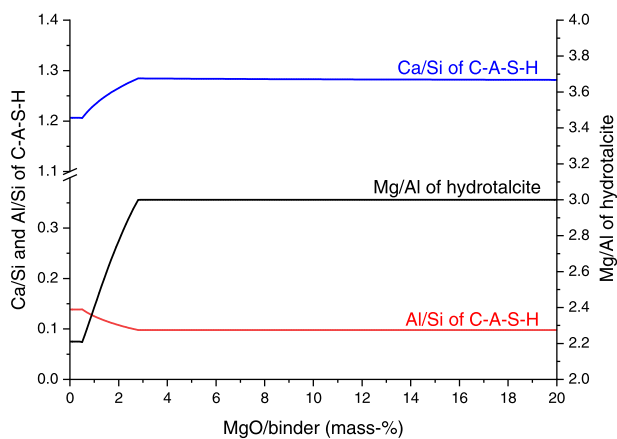
3.5. Thermodynamic modelling

The calculated phase assemblage of the MgO-activated slag, as a function of the MgO dosage, is shown in Fig. 6 (a). The amount of unreacted slag estimated from the deconvolution of ^{29}Si MAS NMR spectra of the samples was used to calculate the phase assemblage, and the degree of reaction was interpolated from 0 to 20% MgO dosage by linear regression. Similarly, the residual MgO quantified by the quantitative XRD analysis was described using a second order polynomial as a function of the MgO dosage. It is noted that strätlingite is present in a minor quantity and stable when the MgO amount is <0.5%. C-A-S-H, the hydrotalcite-like LDH and ettringite are predicted as the major hydration products of the system, and a minor quantity of monocarbonate and calcite are also present throughout the simulated range of the MgO/binder ratios. The stability and thermodynamic preference of monocarbonate can be due to the fact that the kinetics of calcite dissolution is not considered in the thermodynamic modelling, while the formation of hemicarbonate as identified in the XRD pattern of the 0% MgO sample can be due to the slower dissolution rate of calcite, which would stabilize hemicarbonate over monocarbonate.

The volume of ettringite presents a marginal decrease as a function of the MgO dosage, while the volumetric increase of other major phases C-A-S-H, brucite and the hydrotalcite-like phase is more pronounced. This result supports the ^{27}Al MAS NMR results and suggests that a relative increase in the intensity due to the presence of LDH and AFm phases (or a relative decrease in the intensity of ettringite) as observed in the ^{27}Al MAS NMR results can be due to the precipitation of the hydrotalcite-like phase. Moreover, the potential decrease of Al/Si in C-A-S-H at higher MgO dosage as suggested by the ^{27}Al MAS NMR is also found possible according to the thermodynamic calculation of the gel composition of C-A-S-H shown in Fig. 6 (b).
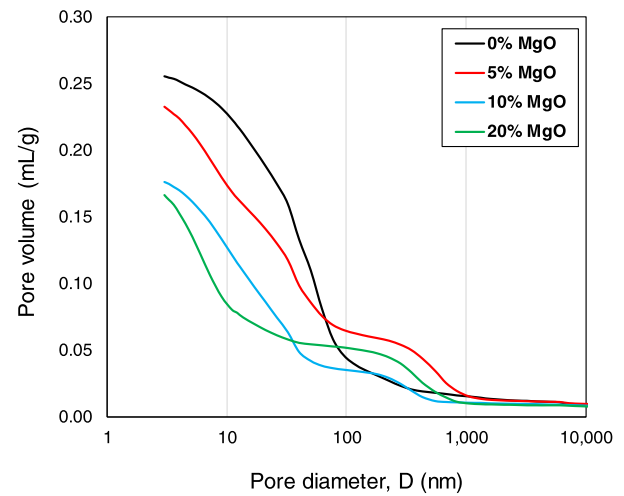
The thermodynamic calculation suggests that the chemical composition of C-A-S-H and the hydrotalcite-like phase notably change up to 3% MgO/binder (Fig. 6 (b)), showing that the Ca/Si and Al/Si ratios of C-A-S-H are predicted to increase from 1.20 to 1.28 and decrease from 0.14 to 0.098, respectively, and the Mg/Al of the hydrotalcite-like phase increases from 2.2 to 2.9. Both the Ca/Si of C-A-S-H and Mg/Al of the hydrotalcite-like phase are much higher than those expected in the slag activated with Na-activators (i.e., $\approx$ 1 and $\approx$ 2.3, respectively [7]). Note that the volume of these phases are expected to continuously increase after this dosage, despite that their chemical compositions are predicted to remain mostly constant after this dosage, as the upper/lower limits for the chemical compositions of the respective phases are reached.

Table 2
Deconvolution results for ^{29}Si MAS NMR spectra of MgO-activated slag samples.

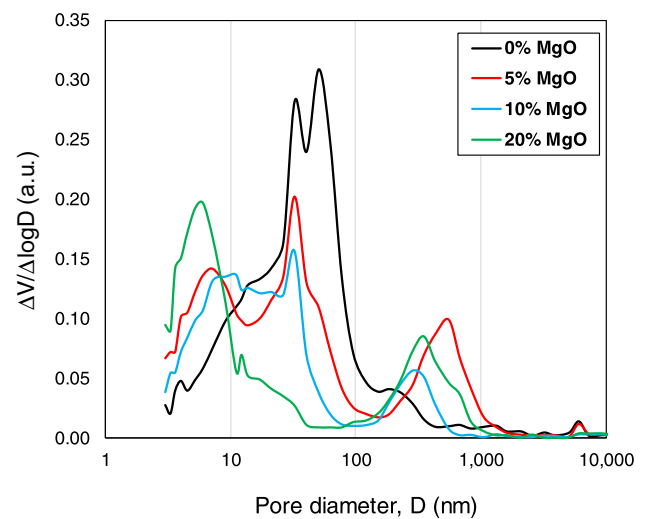| Sample	Unreacted slag	Reaction products						
		Q^0 −73 ppm	Q^1(I) −78 ppm	Q^1(II) −81 ppm	Q^2(1Al) −84 ppm	Q^2 −86 ppm	Q^3(1Al) −89 ppm	Q^4(nAl) −93 ppm
Raw slag	100	–	–	–	–	–	–	–
0% MgO	85	5	4	3	3	–	–	–
5% MgO	86	4	2	5	3	–	–	–
10% MgO	62	8	10	5	11	2	1	2
20% MgO	58	6	10	11	10	2	2	1

(a)

(b)

Fig. 6. Simulated (a) phase assemblage of MgO-activated slag and (b) chemical compositions of C-A-S-H and the hydrotalcite-like LDH as a function of MgO dosage.

The role of MgO used as a chemical activator for slag can be described as changing the compositions of the reaction products at the dosage below 3% by mass, while it is mainly associated with increasing the dissolution of slag at higher dosage. The enhanced dissolution of slag at higher MgO dosage can be due to the increased pH in the pore solution.

The volume occupied by the solid reaction products was higher at increased MgO dosage, implying that increased MgO would lead to a higher degree of hydration and less porosity. Hence, there is potential for higher strength to be attained in the samples with more MgO if the classical gel-space ratio holds for these cements [56].

3.6. MIP

The cumulative pore volume curves of the MgO-activated slag shown in Fig. 7 (a) decrease as the MgO dosage is increased. This agrees with the thermodynamic modeling results which predicted more volume of the solid binder due to the enhancement of the degree of hydration by MgO incorporation. The reduction in the pore volume of the samples is thus attributed to the higher degree of hydration, which led to a higher volume of hydrates present in the matrix.

The first derivatives of the cumulative pore volume curves are shown in Fig. 7 (b). The pores in the 0% MgO sample showed dominant pore populations at effective entry diameters of 32 and 50 nm. The pores with diameters of 10–100 nm were reduced with

(a)

(b)

Fig. 7. (a) Cumulative pore volume and (b) first derivatives of cumulative curves of MgO-activated slag.
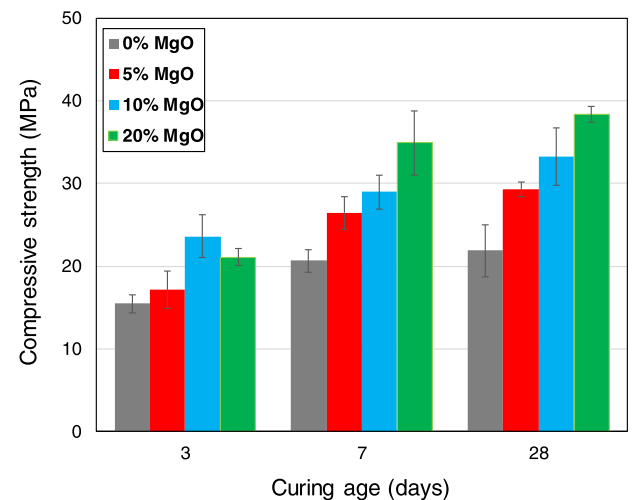

Fig. 8. Compressive strength of MgO-activated slag at 3, 7 and 28 days. The error bars indicate one standard deviation at either side of the mean of three samples.

increasing dosage of MgO, and the pore size distribution of the 20% MgO sample in particular showed no dominant feature at this region. Instead, the MgO-activated samples showed increased porosity at diameters of < 10 and 100–1,000 nm. It is interesting that pores with larger diameters were present in the samples activated by MgO, which leads to formation of more hexagonal hydrates, brucite, and may increase the pore volume in this diameter range as similar with the case of portlandite in hydrated Portland cement [58–59].

3.7. Compressive strength

The compressive strengths of the MgO-activated slag cements at 3, 7, and 28 days are shown in Fig. 8. The samples showed an increase in strength as a function of curing time, constantly increasing until 28 days. Higher MgO dosage also led to an increase in the strength (except at 3 days). A similar result can be found in [60], where it was reported that the strength of slag activated by reactive MgO at 28 days was highest when the MgO dosage was 20%, while that at 90 days was surpassed by the sample with 10% MgO.

The strength increase of the samples upon MgO addition is attributed to the reduction of reduction due to the enhanced degree of hydration, mainly leading to the formation of C-A-S-H along with some ancillary phases (e.g. brucite) in the binder matrix.

4. Conclusion

The hydration kinetics of MgO-activated slag was investigated by employing multiple analytical characterization techniques and a thermodynamic modelling approach. The hydration products of MgO-activated slag system are identified as a C-A-S-H type gel, ettringite, monosulfate, hydrotalcite, brucite, and a third aluminate hydrate. Higher dosage of MgO increased the degree of reaction of slag, and significantly altered the hydration products formed in the system. In particular, a higher population of Al was present in the octahedral region than in the tetrahedral region, due to a potential decrease in the Al uptake by the C-S-H type gel, and greater competition for Al for the formation of the hydrotalcite-like LDH. The phase assemblage predicted by the thermodynamic modelling generally showed fair agreement with the experimental observations, while the formation of hydrotalcite in the present model was not significantly increased by higher MgO dosage, unlike the experimental findings. The cumulative pore volumes of the samples decreased as the MgO dosage was increased, showing close agreement with the thermodynamic modelling results, and are well correlated with the measured strength. Consequently, the strength increase of the samples upon MgO addition can be attributed to the porosity reduction due to enhanced degree of hydration, leading to the formation of C-A-S-H along with some ancillary phases.

CRediT authorship contribution statement

Solmoi Park: Writing - original draft, Conceptualization, Methodology. **Hyeong Min Park:** Data curation, Investigation. **H.N. Yoon:** Data curation. **Joonho Seo:** Visualization. **Cheol-Min Yang:** Validation, Formal analysis. **John L. Provis:** Writing - review & editing. **Beomjoo Yang:** Writing - review & editing, Supervision.

Declaration of Competing Interest

The authors declare that they have no known competing financial interests or personal relationships that could have appeared to influence the work reported in this paper.

Acknowledgments

Appendix A. Rietveld analysis

The XRD patterns of the samples were simulated by refining the scale factor, cell parameters, peak profiles and preferred orientation, as shown in Fig. A1. Phases used in the analysis are listed in Table A1 along with their PDF numbers. CeO_2 (SRM 674b, NIST) was used as an external standard. The background was described using the first-order Chebyshev function coupled with a $1/x$ term. The background in the XRD pattern of the raw slag was described using a polynomial function. The anhydrous slag and C-A-S-H were fitted using arbitrary phases, respectively, which were obtained by whole pattern fitting to improve the fitting results. The obtained phase assemblage was normalized to g/100 g of binder by correcting it for the bound water as measured by the TG (Table A2).
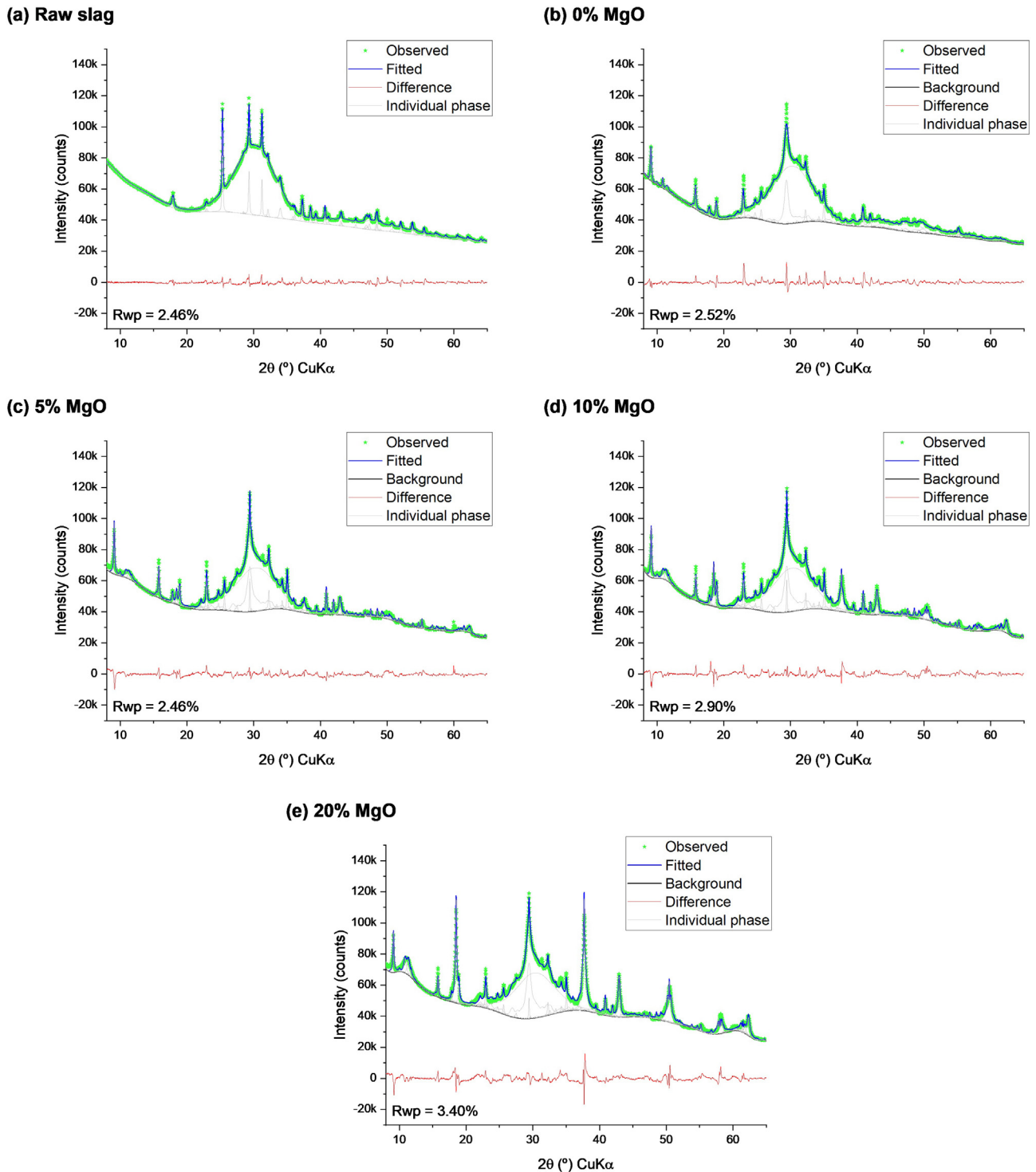
(a) Raw slag

(b) 0% MgO

(c) 5% MgO

(d) 10% MgO

(e) 20% MgO

Fig. A1. Decomposition of the Rietveld analysis of the samples.

Appendix B. Quantification of brucite

The mass of brucite formed in the samples was obtained by the thermodynamic modelling, Rietveld analysis and the TG, as shown in Fig. B1. The obtained quantitative results for brucite were normalized to g/100 g of the binder by correcting for the bound water as measured by the TG. The mass of brucite was obtained from the DTG curve using the tangential method by integrating the area under the mass loss hump due to dehydroxylation of $Mg(OH)_2$ centered at 360–400 °C. The mass of brucite quantified by the TG gives a value notably higher than that obtained by the other two methods, indicating that it can be contributed by the dehydroxylation of the brucite-like layer in the hydrotalcite-like phase.

Table A1
Phases used in the Rietveld analysis.

Phase	Chemical formula	PDF no.
Lime	CaO	43–1001
Portlandite	Ca(OH)$_2$	4–733
Anhydrite	CaSO$_4$	37–1496
Calcite	CaCO$_3$	5–586
Ettringite	Ca$_6$Al$_2$(SO$_4$)$_3$(OH)$_{12}$·26H$_2$O	41–1451
Hemicarbonate	Ca$_4$Al$_2$(OH)$_{12}$(OH)(CO$_3$)$_{0.5}$·5H$_2$O	41–0221
Monocarbonate	Ca$_4$Al$_2$(OH)$_{12}$ (CO$_3$) ·5H$_2$O	01–087-0493
Hydrotalcite	Mg$_2$Al(OH)$_6$(CO$_3$)$_{0.5}$·1.5H$_2$O	01–089-0460
Periclase	MgO	43–1002
Brucite	Mg(OH)$_2$	7–239

Table A2
Phase assemblage of the samples in the unit of g/100 g of binder.

Phase	Raw slag	0% MgO	5% MgO	10% MgO	20% MgO
Lime	0.5				
Portlandite	0.5				
Anhydrite	2.1				
Calcite	1.2		0.7	0.7	0.5
Ettringite		4.1	5.1	4.6	3.8
Hemicarbonate		0.3	0.3	0.5	0.9
Monocarbonate			0.5	0.6	0.7
Hydrotalcite		0.3	0.3	0.6	1.0
Periclase			0.9	1.6	2.7
Brucite			0.9	3.6	10.3
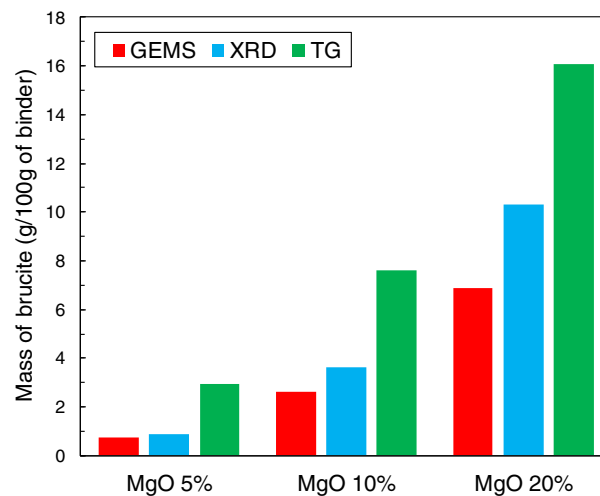
Fig. B1. Mass of brucite obtained by the thermodynamic modelling (GEMS), quantitative XRD analysis and TG.

Appendix C. Deconvoluted ^{29}Si MAS NMR spectra

The ^{29}Si MAS NMR spectra for the MgO-activated samples shown in Fig. C1 was decomposed using the OriginPro 9 software by introducing a component peak at the chemical shift where the relevant Si sites are known to resonate (e.g., [21,25,45,61]). The component peaks were simulating using the Gaussian function, while the spectrum of the raw slag and its resonance in the hydrated samples were simulating the GaussianLortentz function built in the software.
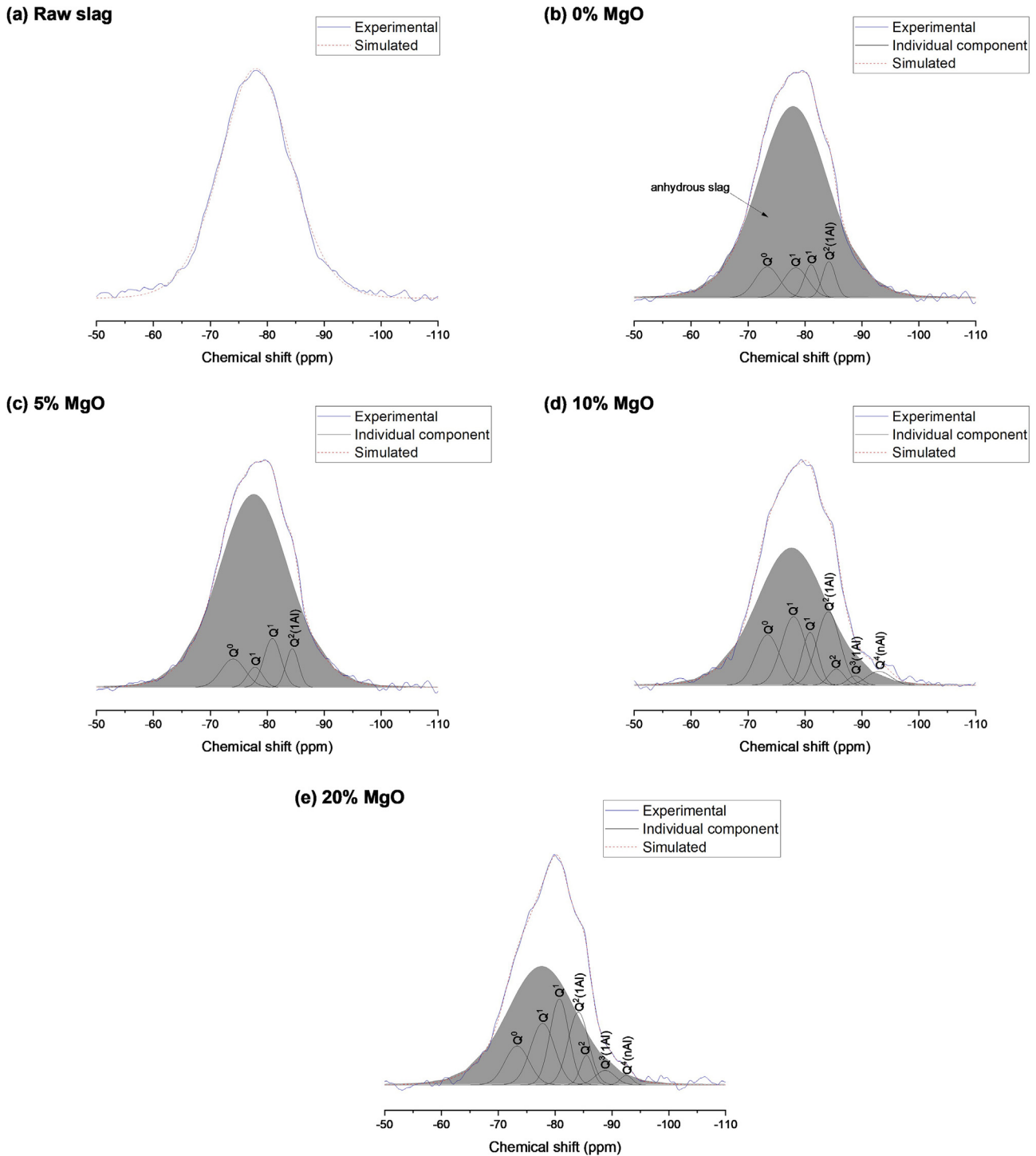
Fig. C1. Decomposed ^{29}Si MAS NMR spectra of the raw slag and the MgO-activated slag samples.

References

[1] R. Snellings, G. Mertens, J. Elsen, Supplementary cementitious materials, Rev. Mineral. Geochem. 74 (1) (2012) 211–278.

[2] M. Juenger, F. Winnefeld, J.L. Provis, J. Ideker, Advances in alternative cementitious binders, Cem. Concr. Res. 41 (12) (2011) 1232–1243.

[3] J.L. Provis, Alkali-activated materials, Cem. Concr. Res. 114 (2018) 40–48.

[4] R. Dhir, M. El-Mohr, T. Dyer, Chloride binding in GGBS concrete, Cem. Concr. Res. 26 (12) (1996) 1767–1773.

[5] M. Criado, J.L. Provis, Alkali activated slag mortars provide high resistance to chloride-induced corrosion of steel, Front. Mater. 5 (34) (2018).

[6] S.M. Park, B. Yang, B. Kim, S. Ha, H.-K. Lee, Structural strengthening and damage behaviors of hybrid sprayed fiber-reinforced polymer composites containing carbon fiber cores, Int. J. Damage Mech. 26 (2) (2017) 358–376.

[7] R.J. Myers, B. Lothenbach, S.A. Bernal, J.L. Provis, Thermodynamic modelling of alkali-activated slag cements, Appl. Geochem. 61 (2015) 233–247.

[8] R. Taylor, I. Richardson, R. Brydson, Composition and microstructure of 20-year-old ordinary Portland cement–ground granulated blast-furnace slag blends containing 0 to 100% slag, Cem. Concr. Res. 40 (7) (2010) 971–983.

[9] B. Yang, K. Cho, G. Kim, H.-K. Lee, Effect of CNT agglomeration on the electrical conductivity and percolation threshold of nanocomposites: a micromechanics-based approach, CMES-Comput. Model. Eng. Sci 103 (5) (2014) 343–365.

[10] D.P. Prentice, S.A. Bernal, M. Bankhead, M. Hayes, J.L. Provis, Phase evolution of slag-rich cementitious grouts for immobilisation of nuclear wastes, Adv. Cem. Res. 1–16 (2018).

[11] B. Lothenbach, K. Scrivener, R. Hooton, Supplementary cementitious materials, Cem. Concr. Res. 41 (12) (2011) 1244–1256.

[12] R.J. Myers, S.A. Bernal, J.L. Provis, Phase diagrams for alkali-activated slag binders, Cem. Concr. Res. 95 (2017) 30–38.

[13] S.A. Bernal, Advances in near-neutral salts activation of blast furnace slags, RILEM Technical Letters 1 (2016) 39–44.

[14] M.S. Kim, Y. Jun, C. Lee, J.E. Oh, Use of CaO as an activator for producing a price-competitive non-cement structural binder using ground granulated blast furnace slag, Cem. Concr. Res. 54 (2013) 208–214.

[15] N. Mobasher, S.A. Bernal, O.H. Hussain, D.C. Apperley, H. Kinoshita, J.L. Provis, Characterisation of Ba (OH) 2–Na2SO4–blast furnace slag cement-like composites for the immobilisation of sulfate bearing nuclear wastes, Cem. Concr. Res. 66 (2014) 64–74.

[16] N. Mobasher, S.A. Bernal, J.L. Provis, Structural evolution of an alkali sulfate activated slag cement, J. Nucl. Mater. 468 (2016) 97–104.

[17] A. Rashad, Y. Bai, P. Basheer, N. Milestone, N. Collier, Hydration and properties of sodium sulfate activated slag, Cem. Concr. Compos. 37 (2013) 20–29.

[18] S.A. Bernal, J.L. Provis, R.J. Myers, R. San Nicolas, J.S. van Deventer, Role of carbonates in the chemical evolution of sodium carbonate-activated slag binders, Mater. Struct. 48 (3) (2015) 517–529.

[19] H. Jeon, J. Yu, H. Lee, G. Kim, J.W. Kim, Y.C. Jung, C.-M. Yang, B. Yang, A combined analytical formulation and genetic algorithm to analyze the nonlinear damage responses of continuous fiber toughened composites, Comput. Mech. 60 (3) (2017) 393–408.

[20] X. Ke, S.A. Bernal, J.L. Provis, Controlling the reaction kinetics of sodium carbonate-activated slag cements using calcined layered double hydroxides, Cem. Concr. Res. 81 (2016) 24–37.

[21] M.B. Haha, B. Lothenbach, G. Le Saout, F. Winnefeld, Influence of slag chemistry on the hydration of alkali-activated blast-furnace slag—Part I: Effect of MgO, Cem. Concr. Res. 41 (9) (2011) 955–963.

[22] S.A. Bernal, J.L. Provis, Durability of Alkali-Activated Materials: Progress and Perspectives, J. Am. Ceram. Soc. 97 (4) (2014) 997–1008.

[23] J.L. Provis, S.A. Bernal, Geopolymers and related alkali-activated materials, Annu. Rev. Mater. Res. 44 (2014) 299–327.

[24] S. Park, J. Jang, H. Lee, Unlocking the role of MgO in the carbonation of alkali-activated slag cement,, Inorg. Chem. Front. 5 (7) (2018) 1661–1670.

[25] S.A. Bernal, R. San Nicolas, R.J. Myers, R.M. de Gutiérrez, F. Puertas, J.S. van Deventer, J.L. Provis, MgO content of slag controls phase evolution and structural changes induced by accelerated carbonation in alkali-activated binders, Cem. Concr. Res. 57 (2014) 33–43.

[26] H. Yoon, S. Park, H. Lee, Effect of MgO on chloride penetration resistance of alkali-activated binder, Constr. Build. Mater. 178 (2018) 584–592.

[27] X. Ke, S.A. Bernal, J.L. Provis, Uptake of chloride and carbonate by Mg-Al and Ca-Al layered double hydroxides in simulated pore solutions of alkali-activated slag cement, Cem. Concr. Res. 100 (2017) 1–13.

[28] O. Burciaga-Díaz, I. Betancourt-Castillo, Characterization of novel blast-furnace slag cement pastes and mortars activated with a reactive mixture of MgO-NaOH, Cem. Concr. Res. 105 (2018) 54–63.

[29] F. Jin, A. Al-Tabbaa, Strength and drying shrinkage of slag paste activated by sodium carbonate and reactive MgO, Constr. Build. Mater. 81 (2015) 58–65.

[30] F. Jin, K. Gu, A. Al-Tabbaa, Strength and drying shrinkage of reactive MgO modified alkali-activated slag paste, Constr. Build. Mater. 51 (2014) 395–404.

[31] F. Jin, K. Gu, A. Al-Tabbaa, Strength and hydration properties of reactive MgO-activated ground granulated blastfurnace slag paste, Cem. Concr. Compos. 57 (2015) 8–16.

[32] M.A. Shand, The Chemistry and Technology of Magnesia, John Wiley & Sons, 2006.

[33] D.A. Kulik, T. Wagner, S.V. Dmytrieva, G. Kosakowski, F.F. Hingerl, K.V. Chudnenko, U.R. Berner, GEM-Selektor geochemical modeling package: revised algorithm and GEMS3K numerical kernel for coupled simulation codes, Comput. Geosci. 17 (1) (2013) 1–24.

[34] T. Wagner, D.A. Kulik, F.F. Hingerl, S.V. Dmytrieva, GEM-Selektor geochemical modeling package: TSolMod library and data interface for multicomponent phase models, Can. Mineral. 50 (5) (2012) 1173–1195.

[35] B. Yang, H. Shin, H. Kim, H.-K. Lee, Strain rate and adhesive energy dependent viscoplastic damage modeling for nanoparticulate composites: Molecular dynamics and micromechanical simulations, Appl. Phys. Lett. 104 (10) (2014) 101901.

[36] B. Lothenbach, D.A. Kulik, T. Matschei, M. Balonis, L. Baquerizo, B. Dilnesa, G.D. Miron, R.J. Myers, Cemdata18: A chemical thermodynamic database for hydrated Portland cements and alkali-activated materials, Cem. Concr. Res. 115 (2019) 472–506.

[37] H.C. Helgeson, D.H. Kirkham, G.C. Flowers, Theoretical prediction of the thermodynamic behavior of aqueous electrolytes by high pressures and temperatures; IV, Calculation of activity coefficients, osmotic coefficients, and apparent molal and standard and relative partial molal properties to 600 degrees C and 5kb, Am. J. Sci. 281 (10) (1981) 1249–1516.

[38] S.A. Bernal, J.L. Provis, B. Walkley, R. San Nicolas, J.D. Gehman, D.G. Brice, A.R. Kilcullen, P. Duxson, J.S. van Deventer, Gel nanostructure in alkali-activated binders based on slag and fly ash, and effects of accelerated carbonation, Cem. Concr. Res. 53 (2013) 127–144.

[39] H. Park, Y. Jeong, J.-H. Jeong, J.E. Oh, Strength development and hydration behavior of self-activation of commercial ground granulated blast-furnace slag mixed with purified water, Materials 9 (3) (2016) 185.

[40] H.F. Taylor, Cement chemistry, Thomas Telford1997.

[41] M. Maciejewski, H.-R. Oswald, A. Reller, Thermal transformations of vaterite and calcite, Thermochim. Acta 234 (1994) 315–328.

[42] J. Cho, S.-K. Lee, S.-H. Eem, J.G. Jang, B. Yang, Enhanced mechanical and thermal properties of carbon fiber-reinforced thermoplastic polyketone composites, Compos. A Appl. Sci. Manuf. 126 (2019) 105599.

[43] F.L. Theiss, G.A. Ayoko, R.L. Frost, Thermogravimetric analysis of selected layered double hydroxides, J. Therm. Anal. Calorim. 112 (2) (2013) 649–657.

[44] R. Trittschack, B. Grobéty, P. Brodard, Kinetics of the chrysotile and brucite dehydroxylation reaction: a combined non-isothermal/isothermal thermogravimetric analysis and high-temperature X-ray powder diffraction study, Phys. Chem. Miner. 41 (3) (2014) 197–214.

[45] R.J. Myers, S.A. Bernal, J.D. Gehman, J.S. Deventer, J.L. Provis, The Role of Al in Cross-Linking of Alkali-Activated Slag Cements, J. Am. Ceram. Soc. 98 (3) (2015) 996–1004.

[46] G. Sun, J.F. Young, R.J. Kirkpatrick, The role of Al in C-S-H: NMR, XRD, and compositional results for precipitated samples, Cem. Concr. Res. 36 (1) (2006) 18–29.

[47] P. Faucon, A. Delagrave, J. Petit, C. Richet, J. Marchand, H. Zanni, Aluminum incorporation in calcium silicate hydrates (C− S− H) depending on their Ca/Si ratio, J. Phys. Chem. B 103 (37) (1999) 7796–7802.

[48] X. Pardal, F. Brunet, T. Charpentier, I. Pochard, A. Nonat, 27Al and 29Si solid-state NMR characterization of calcium-aluminosilicate-hydrate, Inorg. Chem. 51 (3) (2012) 1827–1836.

[49] J. Cho, H.G. Jang, S.Y. Kim, B. Yang, Flexible and coatable insulating silica aerogel/polyurethane composites via soft segment control, Compos. Sci. Technol. 171 (2019) 244–251.

[50] M.D. Andersen, H.J. Jakobsen, J. Skibsted, A new aluminium-hydrate species in hydrated Portland cements characterized by 27 Al and 29 Si MAS NMR spectroscopy, Cem. Concr. Res. 36 (1) (2006) 3–17.

[51] S.-D. Wang, K.L. Scrivener, 29 Si and 27 Al NMR study of alkali-activated slag, Cem. Concr. Res. 33 (5) (2003) 769–774.

[52] A. Brough, A. Atkinson, Sodium silicate-based, alkali-activated slag mortars: Part I. Strength, hydration and microstructure, Cem. Concr. Res. 32 (6) (2002) 865–879.

[53] I.G. Richardson, A.R. Brough, R. Brydson, G.W. Groves, C.M. Dobson, Location of aluminum in substituted calcium silicate hydrate (C-S-H) gels as determined by 29Si and 27Al NMR and EELS, J. Am. Ceram. Soc. 76 (9) (1993) 2285–2288.

[54] G. Le Saoût, M. Ben Haha, F. Winnefeld, B. Lothenbach, Hydration Degree of Alkali-Activated Slags: A 29Si NMR Study, J. Am. Ceram. Soc. 94 (12) (2011) 4541–4547.

[55] M.B. Haha, G. Le Saout, F. Winnefeld, B. Lothenbach, Influence of activator type on hydration kinetics, hydrate assemblage and microstructural development of alkali activated blast-furnace slags, Cem. Concr. Res. 41 (3) (2011) 301–310.

[56] T.C. Powers, Structure and physical properties of hardened Portland cement paste, J. Am. Ceram. Soc. 41 (1) (1958) 1–6.

[57] P.K. Mehta, P.J. Monteiro, Concrete microstructure, properties and, materials (2017).

[58] J. Jang, H. Lee, Microstructural densification and CO2 uptake promoted by the carbonation curing of belite-rich Portland cement, Cem. Concr. Res. 82 (2016) 50–57.

[59] H.M. Park, S. Park, S.-M. Lee, I.-J. Shon, H. Jeon, B. Yang, Automated generation of carbon nanotube morphology in cement composite via data-driven approaches, Compos. B Eng. 167 (2019) 51–62.

[60] Y. Yi, X. Zheng, S. Liu, A. Al-Tabbaa, Comparison of reactive magnesia-and carbide slag-activated ground granulated blastfurnace slag and Portland cement for stabilisation of a natural soil, Appl. Clay Sci. 111 (2015) 21–26.

[61] M. Palacios, F. Puertas, Effect of carbonation on alkali-activated slag paste, J. Am. Ceram. Soc. 89 (10) (2006) 3211–3221.

[62] J.H. Seo, S.M. Park, H.K. Lee, Evolution of the binder gel in carbonation-cured Portland cement in an acidic medium, Cem. Concr. Res. 109 (2018) 81–89.

[63] S. Park, H.N. Yoon, J.H. Seo, H.K. Lee, J.G. Jang, Structural evolution of binder gel in alkali-activated cements exposed to electrically accelerated leaching conditions, J. Hazard. Mater. 387 (2020) 121825.

[64] S.M. Park, J.G. Jang, Carbonation-induced weathering effect on cesium retention of cement paste, J. Nucl. Mater. 505 (2018) 159–164.